Soft tubular microfluidics for 2D and 3D applications

Wang Xi[a,b,1], Fang Kong[c,1], Joo Chuan Yeo[d,e,1], Longteng Yu[d], Surabhi Sonam[b,d], Ming Dao[c], Xiaobo Gong[f,g,h,2], and Chwee Teck Lim[a,b,c,d,e,2]

[a]Centre for Advanced 2D Materials and Graphene Research Centre, National University of Singapore, Singapore 117546; [b]Mechanobiology Institute, National University of Singapore, Singapore 117411; [c]Singapore-Massachusetts Institute of Technology Alliance of Research and Technology, National University of Singapore, Singapore 117548; [d]Department of Biomedical Engineering, National University of Singapore, Singapore 117583; [e]National University of Singapore Graduate School of Integrative Sciences and Engineering, National University of Singapore, Singapore 117456; [f]Ministry of Education Key Laboratory of Hydrodynamics, Department of Engineering Mechanics, School of Naval Architecture, Ocean and Civil Engineering, Shanghai Jiao Tong University, Shanghai 200240, China; [g]SJTU-CU (Shanghai Jiao Tong University-Chiba University) International Cooperative Research Center, School of Naval Architecture, Ocean and Civil Engineering, Shanghai Jiao Tong University, Shanghai 200240, China; and [h]Collaborative Innovation Center for Advanced Ship and Deep Sea Exploration, School of Naval Architecture, Ocean and Civil Engineering, Shanghai Jiao Tong University, Shanghai 200240, China

Microfluidics has been the key component for many applications, including biomedical devices, chemical processors, microactuators, and even wearable devices. This technology relies on soft lithography fabrication which requires cleanroom facilities. Although popular, this method is expensive and labor-intensive. Furthermore, current conventional microfluidic chips precludes reconfiguration, making reiterations in design very time-consuming and costly. To address these intrinsic drawbacks of microfabrication, we present an alternative solution for the rapid prototyping of microfluidic elements such as microtubes, valves, and pumps. In addition, we demonstrate how microtubes with channels of various lengths and cross-sections can be attached modularly into 2D and 3D microfluidic systems for functional applications. We introduce a facile method of fabricating elastomeric microtubes as the basic building blocks for microfluidic devices. These microtubes are transparent, biocompatible, highly deformable, and customizable to various sizes and cross-sectional geometries. By configuring the microtubes into deterministic geometry, we enable rapid, low-cost formation of microfluidic assemblies without compromising their precision and functionality. We demonstrate configurable 2D and 3D microfluidic systems for applications in different domains. These include microparticle sorting, microdroplet generation, biocatalytic micromotor, triboelectric sensor, and even wearable sensing. Our approach, termed soft tubular microfluidics, provides a simple, cheaper, and faster solution for users lacking proficiency and access to cleanroom facilities to design and rapidly construct microfluidic devices for their various applications and needs.

flexible microfluidics | elastomeric microtubes | microfluidic assemblies | inertial focusing chip | microfluidic sensor

Poly(dimenthylsiloxane) (PDMS)-based microfluidic systems are the key components for applications ranging from manipulation and sorting of microentities, tissue engineering, biochemical analysis to wearable sensing (1–4). The ability of microfluidics to manipulate minute amounts of liquids for rapid screening is one of the most compelling reasons for their use. Despite these advantages, the construction of such microfluidic systems using the conventional lithography method is not trivial (5, 6). Typically, the microfabrication process involves expensive and time-consuming cleanroom-based photolithography techniques to pattern microscale features on a planar substrate. PDMS prepolymer is then cast into the mold to yield a polymeric replica. Next, the surface of this replica together with another flat substrate are surface-treated and brought into contact to form closed channels. While this method forms well-defined microstructures of various topographies (7), it has obvious limitations. For example, one major drawback is that it is limited to microchannels in a 2D planar layout. As such, fabrication of complex 3D microfluidic systems involves multiple steps of aligning, stacking, and bonding multiple layers and components together (6, 8). Also, these 3D arrangements require elements such as microvalves, pumps (8, 9), and interconnectors to enable deterministic fluid streams. Moreover, even though a soft lithography process was introduced more than two decades ago (10), this

process is still labor-intensive, further increasing production cost (6). In addition, design reiterations require the entire fabrication process to be repeated. Apart from these, the current soft lithography method is limited to microchannels with rectangular cross-sections (10). This affects the study of biological applications, as the sharp edges do not recapitulate the circular internal surfaces such as blood capillaries (11). To perform accurate studies to investigate vascular processes (12) and for mimicking in vivo hydrodynamics (11), microchannels with circular cross-sections would be much more suitable, but are difficult to achieve using current photolithography methods.

To circumvent these difficulties, several cleanroom-free approaches have been proposed for creating microfluidic systems with various channel geometries, including computer numerical control milling (13), laser cutting (14), and hot embossing (15). However, these techniques require expensive equipment, and are limited to planar manufacturing. Another emerging strategy is 3D printing (6, 16, 17). Generally, 3D microcavity networks are formed either by printing 3D sacrificial filament templates that are later leached away after prototyping (17) or by polymerizing the walls of the channel cavities followed by drainage of the uncured photopolymer precursor (16). Particularly, in one approach exploiting stereolithography rapid prototyping, modular and reconfigurable components containing fluidic elements are manufactured to allow rapid assembly of channels for 3D routing (18). Although attractive,

---

Significance

The current cleanroom-based soft lithography microfabrication process is complicated and expensive. There is a need for low-cost, ready-to-use, modular components that can be easily assembled into microfluidic devices by users lacking proficiency or access to microfabrication facilities. We present a facile, low-cost, and efficient method of fabricating soft, elastic microtubes with different cross-sectional shapes and dimensions. These microtubes can be used as basic building blocks for the rapid construction of various 2D and 3D microfluidic devices with complex geometries, topologies, and functions. This approach avoids the conventional cumbersome photolithography process and thus, provides a feasible way for scaling up the production of microfluidic devices.

---

extrusion-based 3D printers suffer from poor printing resolution at scales larger than 50 μm, depending on the nozzle size and printing pressure (6). For laser-assisted 3D printing techniques, the choice of materials is restricted to photopolymers and UV-curable resins (19), and the surface roughness due to laser beam overcuring also raises concerns with regard to high-resolution imaging within the channels (6). Using another approach, Lee et al. (20) demonstrated a method to fabricate 3D cylindrical micronetworks in PDMS using sucrose sacrificial fibers. Although this protocol is relatively simple, the premade sucrose fiber templates were manually bonded with individual fibers, which is inefficient and error-prone, especially when handling fibers smaller than 30 μm in diameter (20). Altogether, these methodologies do not allow for fast, low-cost, and versatile fabrication of a range of topologically and geometrically complex microfluidic systems.

Here, we present an efficient and economical method of fabricating elastic microfluidic tubings (microtubes) of different cross-sectional geometries using simple mechanical apparatus and commonly available materials in the laboratory. These microtubes are flexible, stretchable, transparent, and biocompatible, and can be made from various elastomeric materials. The capability of epithelialization and endothelialization of the microtube's interior surfaces indicate their potential use for organ-on-chip applications. Moreover, the microtubes form the basic building blocks for microfluidic assemblies for various applications. Importantly, we show that not only can essential microfluidic components such as valves and actuators be quickly formed using the microtubes, but 2D and out-of-plane 3D microchannels can also be built with relative ease. Finally, the versatility of this approach, termed "soft tubular microfluidics" (STmF), for the rapid assembly of functional microfluidic systems is verified via the development of devices for a variety of applications. These applications span different domains, from microparticles separation and droplet generation using physical force fields, to micromotor actuation using biocatalytic reactions, to electrochemical detection using triboelectric principles, and finally to wearable sensing using physicoelectrical phenomenon (Fig. 1).

Results

Fabrication of Elastomeric Microtubes. We developed a continuous extrusion and curing process to produce PDMS elastic microtubes (refer to *Materials and Methods* and Movie S1). Importantly, by drawing an electrically heated metal filament vertically through a pool of PDMS precursor, the viscosity and surface tension led to the coating of PDMS around the metal wire template. This template was further heated and the PDMS cured fully in situ in an electric heating unit to preserve the tubular shape (*SI Appendix*, Fig. S1). The PDMS microtube was then separated from the metal filament via sonication. Fig. 2A shows the elastomeric microtubes of high flexibility and stretchability after the separation. Notably, the whole process is simple and nontoxic, as it does not require the use of harmful chemicals (20). Furthermore, this continuous fabrication process allows for production of microtubes with inner diameters (ID) as small as 10 μm (Fig. 2B) and lengths of more than 50 cm (*SI Appendix*, Fig. S2). In our experimental setup, we produced microtubes with uniform IDs and outer diameters (ODs) (Fig. 2B and *SI Appendix*, Fig. S2). We obtained microtubes with OD/ID = 2:1, 3:1, 4:1, using metal filaments with diameters of 10 μm to 400 μm. Despite their high aspect ratios (length/diameter of ~5,000) and thin walls, the microtubes were robust and did not sag or collapse during handling and use. Compared with other approaches to produce elastomeric microtubes for on-chip applications (12, 21), our technique avoids the complicated procedures for aligning microtemplates to produce microtubes with lumens of comparable scale to most microfluidic channels. Using atomic force microscopy, the microtubes showed smooth inner surfaces after peeling off (*SI Appendix*,
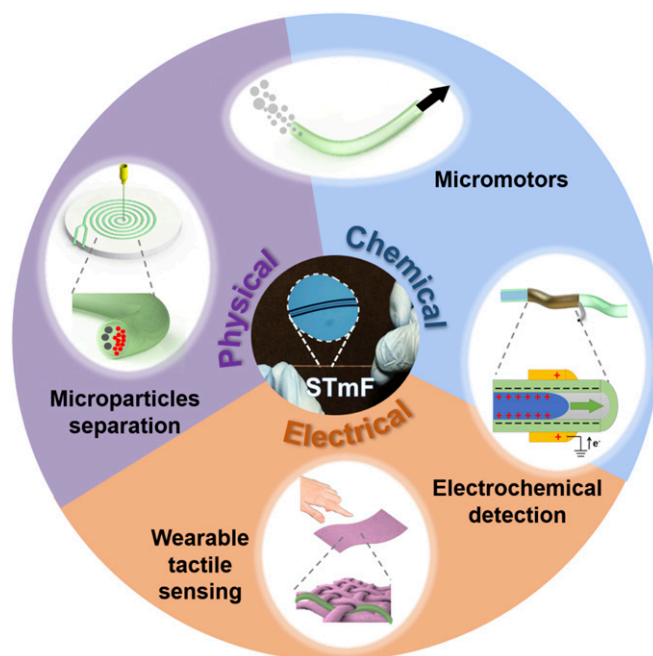

Fig. 1. Soft tubular microfluidics (STmF) applications. Schematic showing the diverse applications of the microtubes in various domains: from microparticles/cells separation and droplet generation using physical force fields, to micromotor actuation using biocatalytic reactions, to triboelectric sensing using electrochemical principles, and finally to wearable sensing using physicoelectrical phenomenon.

Fig. S3). Notably, this allows excellent physical flow fields and optical imaging right inside the microtubes.

Assuming constant temperature, the wall thickness d of the microtube is controlled by the radius of the wire template r, and capillary number Ca, using (22)

$$\frac{d}{r} = \frac{1.34Ca^{2/3}}{1 - 1.34Ca^{2/3}}. \qquad [1]$$

In turn, the capillary number $Ca = \mu V / \sigma$ may be altered with different fabrication conditions, where μ is the dynamic viscosity of PDMS, V is the characteristic velocity of wire drawing, and σ is the surface tension of the liquid. Therefore, microtubes of varying ODs may be easily fabricated. Moreover, the channel cross-section geometry can be adjusted using different filament templates (Fig. 2C). For circular microtubes, we also fabricated microtubes with different materials, such as UV-curable polymer and silicone rubber (*SI Appendix*, Fig. S4), highlighting the versatility of this process.

Fig. 2D describes the ease in assembling elastic microtubes into different configurations. We demonstrated how microtubes with ID = 50 μm can be wound up to form a circle, triangle, rectangle, square, or pentagon (Fig. 2D). Similarly, 3D configurations can also be formed. Here, two channels filled with aqueous solutions of green or red fluorescein were tied into a Carrick bend knot (Fig. 2D, *Bottom Left*). The size of the bend was determined by the ODs of the microtubes, and the entire knot occupied a volume of $0.8 \times 1.5 \times 0.8$ mm³. Other 3D systems such as a double helix (Fig. 2D, *Bottom Right*) were produced by winding two microtubes onto a cylindrical template that positioned the microtubes in a predesigned 3D orientation. Furthermore, multiple lumens may also be built within the same microtubular structure to allow proximal fluid interactions (Fig. 2E). Similarly, microtubes with branched configurations were also fabricated using deterministically designed wire templates. Fig. 2F shows an example of a microtube with bifurcated lumens.
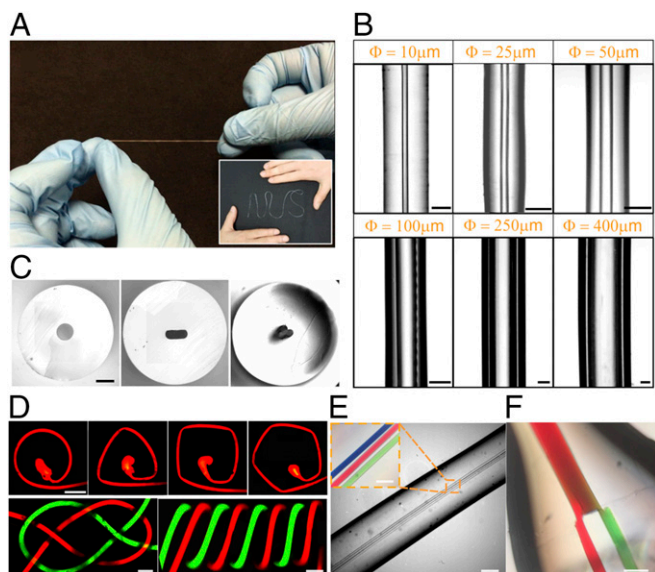
Fig. 2. Fabrication of elastomeric microtubes. (*A*) Photograph of elastomeric microtube, demonstrating its flexibility and stretchability. (*Inset*) A microtube of over 30 cm, patterned to form the term "NUS." (*B*) Images of PDMS microtubes with circular cross-sections with different IDs (side view, IDs are indicated by the orange text). (Scale bars: 30 μm for ID (Φ) = 10 μm, 75 μm for Φ = 25 μm, and 100 μm for the rest.) (*C*) Transverse planes of PDMS tubes with cross-sectional shapes of (*Left*) circle, (*Center*) rectangle, and (*Right*) club. (Scale bar: 250 μm.) (*D*) Microchannels of various 2D and 3D geometries created by winding the PDMS microtubes. (*Top*) Fluorescent images of 2D microchannels in (*Left*) circular, (*Center Left*) rectangular, (*Center Right*) square and (*Right*) pentagonal shapes. (Scale bar: 400 μm.) (*Bottom*) Optical micrographs of 3D microstructures (ID = 50 μm) in the shape of (*Left*) a Carrick bend knot and (*Right*) a double helical. (Scale bar: 150 μm.) (*E*) Microtube with multiple lumens. (*Inset*) Colored dyes within the microchannels. (Scale bars: 400 μm and, for *Inset*, 150 μm.) (*F*) Microtube with a bifurcated microchannel: two smaller channels merging into one main channel. (Scale bar: 200 μm.)

Here, two smaller channels were merged into the main channel. Colored dyes within the lumens suggest consistency and laminar flow at the junction. This can be further iterated to produce a complex network. Furthermore, we included a connector compatible to commercially available syringe tips to facilitate liquid injection (*SI Appendix*, Fig. S5).

Microtubes as Basic Microfluidic Components. The mechanical properties of the PDMS microtubes were characterized and summarized in *SI Appendix*, Table S1. The microtubes possess superior properties compared with commercially available silicon tubing owing to their small size. The microtubes are also highly elastic, stretchable, and robust to withstand high intraluminal pressure above 13 bars (*SI Appendix*, Fig. S6A). Notably, when the intraluminal pressure increased above 10 bar, the IDs of the PDMS microtubes (OD/ID = 3:1) expanded about twofold without plastic deformation (*SI Appendix*, Fig. S6B). To understand how the OD/ID ratio influences the expansion of IDs as a function of intraluminal pressure, we calculated the expansion of the ID for microtubes with various OD/ID ratios using Eq. **2** derived from a theoretical solution (23),

$$D = 1 + \frac{1+\nu}{E}\left(1 + 2\frac{1-\nu}{K^2-1}\right)p, \qquad [2]$$

where D is the expansion ratio, ν is the Poisson's ratio, E is the Young's modulus, K equals OD/ID, and p represents the intraluminal pressure. For a perfect elastic tube, D increases linearly with p (*SI*

Appendix, Fig. S6C). We observed that our experimental data are consistent with the simulation for $K = 3$ when pressure is below 10 bar (*SI Appendix*, Fig. S6D). At higher pressure, the PDMS microtubes reached their elastic limit, resulting in higher discrepancy.

Moreover, the PDMS microtubes possess a low Young's modulus of 1.5 MPa to 2.0 MPa, allowing for significant deformation with applied forces. This property is especially advantageous for valving and fluid actuation. By using a mechanical clamp to pinch the microtubes, the flow may be interrupted (*SI Appendix*, Fig. S7A). Adjusting the clamping frequency of the clamp enables on-demand valving. We observed that the mechanical clamp closes and opens the valve within 5 ms to 16 ms without any lag behind the control signal (*SI Appendix*, Fig. S7 *B* and *C*), which is common in pneumatic valves (8, 24). Notably, the rounded channels are fully occluded at lower compressive force than rectangular and square channels, as reported in previous literature (8). Importantly, no signs of rupture or fatigue were observed after more than 20,000 cycles of actuations, demonstrating the excellent robustness of the microtubes. Similarly, a rotational actuator could be implemented along the length of the microtubes to produce a pulsatile flow (*SI Appendix*, Fig. S7D). By controlling the rotational speed, we achieved a maximum pumping rate of ~100 picoliter per second (*SI Appendix*, Fig. S7 *E* and *F*). In contrast to the complicated multiple-layered microvalve and micropump systems fabricated by soft lithography (8, 9) and stereolithography (24), our valve and pump systems have a much simpler structure and can be easily integrated.

Flow Characteristics Inside Circular Microtubes. Conventional rectangular microchannel is a poor representation of the in vivo vasculature features (11). By simulating the flow profiles of circular and square microchannels (*SI Appendix*, Fig. S8A), we noted that the flow rate is significantly slower in the square channel: 88.31% that of a circular channel with the same cross-sectional area. In particular, the flow velocity was notably slower at the four corners of the square cross-section compared with the same segment at the annulus. This difference accounts for selective migration of the microparticles in the microchannels (25), limiting the accurate mimicking of the in vivo flow of cells through blood capillaries. In our study with circular microtubes, flow conditions in blood vessels can be easily mimicked and studied. To demonstrate this, we flowed whole blood samples mixed with DAPI-stained HeLa cells (0.1% of normal erythrocyte count) into a flexible circular microtube (ID = 25 μm). The migration of the HeLa cells toward the channel walls in the flow (20 μL/min, *SI Appendix*, Fig. S8B) was clearly observed, resembling the in vivo margination effect (26). The hydrodynamic interactions among red blood cells (RBCs), non-RBC cells, and vessel walls result in a flow profile where the RBCs tend to occupy the center of the vessel while the larger cells, including white blood cells and cancer cells, migrated toward the cell-free layer near the walls (27) (*SI Appendix*, Fig. S8C). Insights into such phenomenon will enable better understanding of flows in human circulatory systems and developing better strategies for drug delivery.

Also, the biocompatibility of the microtubes allows the functionalization of their inner surfaces with biomolecules and thus promotes the adherence and growth of epithelial (Madin-Darby canine kidney epithelial, MDCK) and endothelial (Human Umbilical Vein Endothelial Cells, HUVECs) cells. We observed that the cells (indicated by the GFP-tagged or DAPI-stained nuclei) attached to the whole circumference of circular microtubes, forming hollow tubular cell sheets (*SI Appendix*, Fig. S8 *D* and *E*). The merits of transparency, biocompatibility, and flexibility of the microtubes make it possible to investigate in-depth cellular processes under physiological stresses and in vivo-like microenvironments. Collectively, the epithelialization and endothelialization of soft microtubes present a step toward better tissue engineered microfluidic organ-on-a-chip systems.

Assembly of 3D Microfluidic Functional Systems. The microtubes provide versatility to create functional microfluidic elements. Here, we presented various versions of microfluidics for inertial focusing and microdroplet generation. Using PDMS circular microtubes with ID = 100 μm, we designed four different inertial focusing microfluidic chips of either 2D or 3D configuration (Fig. 3*A* and *SI Appendix*, Fig. S9). The deterministic contours of the microtubes were achievable, using 3D printed templates, within minutes (Movie S2). The easy assembly of an inertial focusing microfluidics platform meets the requirements for a simple, low-cost, and high-throughput technique in a variety of clinical, industrial, and analytical applications (28). We used shear- or wall-induced lift forces and lateral Dean drag force (29, 30) to control positions of suspended polystyrene microparticles under flow. Several key factors, including the hydraulic diameter, D_h, the particle size, a, the Dean number, D_e, the radius of curvature of microchannels, and flow velocity, are known to affect particle focusing (29). The radius of the 2D spiral channel curvature increases with turn, while the 3D helix comprises spirals of the same D_e radius, simplifying mathematical calculations. Furthermore, the twisted channel has the highest possible curvature, resulting in high D_e (*SI Appendix*, Fig. S10). The small diameter of our channels enables laminar flow (Reynolds number, $Re \ll 2,300$) even at intermediate flow rate (100 μL/min to 1,200 μL/min), and the designs with different radii of curvature offer a range of D_e suitable for different conditions (*SI Appendix*, Fig. S10).

To test the performance of particle focusing, 1% polystyrene microparticle aqueous suspensions (particles ranging from 10 μm to 25 μm in diameter) were used. We expanded the channels at the outlet by connecting the microtubes to PDMS replicas of pulled glass capillaries with sharp tips. We tracked individual particles (*SI Appendix*, Fig. S11) to optimize the device's focus efficiency, defined as $E = (1 - W_T/W_C)$, where W_T is the width of the projected tracks, and W_C is the width of the channel at the outlet. We observed that, in the range of moderate Dean numbers ($D_e \approx 1–30$), the bead formed narrow streamlines (W_T) of ~10 to 20% of the outlet diameter (*SI Appendix*, Fig. S11). This is consistent with the empirical conditions for particles of $a/D_h > 0.07$ (29), and high focus efficiencies of >78% were calculated for different size particles in various devices (Fig. 3*B* and *SI Appendix*, Fig. S12). Similarly, MCF-10A epithelial cells were focused with an efficiency of ~85% and retrieved using the 3D helical chip (*SI Appendix*, Fig. S13), demonstrating high effectiveness and versatility. Furthermore, we separated polydispersed particles into their respective streamlines in a continuous flow (*SI Appendix*, Fig. S14). Fig. 3*C* shows the lateral displacement of particles with diameters of 10 μm and 25 μm at optimal flow rate (500 μL/min) in a 3D helical chip. Importantly, the split streams allow the particles to be sorted and collected. Under similar conditions, separation of different-sized beads is also achieved with high efficiency (*SI Appendix*, Fig. S15). We provided a flow rate of 500 μL/min, comparable to previously reported high-throughput microfluidic systems (29). Thus, the high performance of our STmF inertial focusing devices shows promise for applications in diagnostic isolation and filtration, including label-free retrieval of circulating tumor cells from whole blood (30).

To generate microdroplets, we use an off-the-shelf fluidic connector to create a microfluidic T-junction (31). Unlike continuous flow systems, droplet-based devices focus on creating discrete volumes in an immiscible phase. Here, a T-junction was implemented by connecting three PDMS tubes to a commercially available plastic fluidic connector. For better imaging of droplet formation, we fabricated a PDMS T-junction by molding a T configuration of two small steel rods. The T-junction was then connected to a microtube of ID = 50 μm for fluid outlet (*SI Appendix*, Fig. S16*A*), and two microtubes of ID = 250 μm were used, one to flow continuous oil fluid and the other to deliver suspended water droplets. In our experiments, the chip generated microdroplets of 200 μm to 500 μm in diameter (*SI Appendix*, Fig. S16*B*) at frequencies ranging from 5 Hz to 1,000 Hz (*SI Appendix*, Fig. S16*C*), with the aqueous and carrier flow rates higher than 1 μL/min and 500 μL/min, respectively. In addition, the outlet of the flexible microtubes could be conveniently connected to another chip or a container to deliver the discrete water droplets on demand, allowing the device to be used as a portable soft microfluidic droplet generator.

Applications in Micromotors, Biochemical Detection, and Tactile Sensing. Beyond microfluidic applications, our fabricated microtubes may be used with other chemicals and accessories to achieve devices fulfilling various needs. For example, self-propelled microscale motors are currently gaining interest, with tremendous potential for biomedical applications and robotics (32). These micromotors may be created by encapsulating accessible fuels, such as hydrogen peroxide, hydrazine, glucose, and acid, which may be catalyzed into mechanical motion (33). To demonstrate this, we created a biocatalytically active surface within the microtubes by functionalizing the inner wall with catalase, an enzyme that efficiently decomposes hydrogen peroxide. We then placed these microtubes into hydrogen peroxide solutions. Upon interaction, the microtube releases oxygen gas internally. Here, the narrow opening at the end of the microtube serves as a propelling outlet during the catalytic reaction of the hydrogen peroxide fuels, resulting in locomotion (Fig. 4*A* and Movie S3). Importantly, by altering the concentration of hydrogen peroxide, we achieved different speeds for the microtube (Fig. 4*B*).
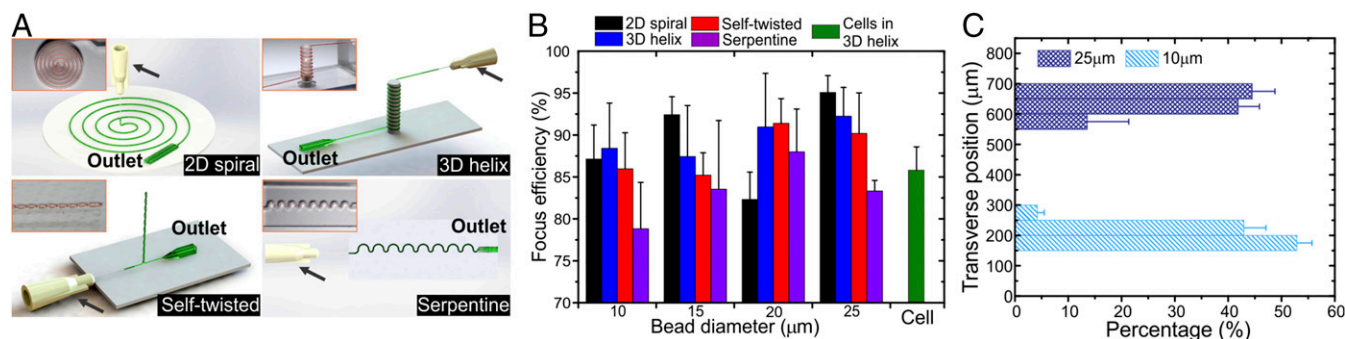
Fig. 3. Microtube-based microfluidic devices for inertial focusing and sorting of microparticles. (*A*) STmF chips in four different configurations for inertial focusing. The microtubes (ID = 100 μm) were wound into planar spiral, 3D spiral around a cylinder, 3D self-twisted, and 2D serpentine configurations (black arrow indicates inlet). (*Insets*) Photos of these channels (encircled by orange boxes). (*B*) Histogram plot presenting the focus efficiency for particles of different diameter and cells tested in various chips. (*C*) Lateral positions of microbeads of 10 μm and 25 μm in diameter (0.5% concentration for each) in the outlet.

Next, microtubes may form the fluid delivery component for electrochemical sensing. Triboelectricity generation has been demonstrated successfully in recent years with the utilization of materials with different triboelectric characteristics (34). Furthermore, a self-powered nanosensor detecting flow rates may be developed based on the coupling of triboelectric effect and electrostatic induction (35). In particular, by analyzing the electrostatic and electrokinetic interactions at the liquid and solid interface, concentrations of different chemical compounds may be detected. To demonstrate this, we attached an electrode around a portion of a PDMS microtube. Due to the triboelectric properties of PDMS and electrostatic induction, positive charges were screened on the electrode. When an electrolyte flowed into the tube, it formed an electric double layer on the inner wall surface (36), which screened the negatively charged PDMS and caused a positive spiked triboelectric current (Fig. 4C). Similarly, when the electrolyte was pumped out of the microtube, it induced a negative spiked current. We want to emphasize that the thin wall of the tube allows efficient electrostatic induction, facilitating the movement of electrons, and enhancing sensing capabilities. As a proof-of-concept, we flowed potassium chloride (KCl) of various concentrations within the tube. Interestingly, we detected triboelectric current pulses even at picomolar concentrations (Fig. 4D), suggesting a highly sensitive microtubular chemical sensor.

Finally, we functionalized our microtubes by dispensing an active sensing element within the microtube. Eutectic gallium indium, a form of liquid metal, has been used previously for various microfluidic applications involving interconnections (37), sensing (38, 39), actuation (40), and heating (41). By dispensing eutectic gallium indium into the microtube, we create an electrical wire that is soft, thin, and stretchable. The one-dimensional soft sensing microtube can be multiplexed and contoured into 3D features for different applications. For example, we developed a wearable fabric touch sensor by weaving multiple functional microtubes into a textile fabric (Fig. 4E). As the microtubular fibers are almost the same diameter as the fabric, they enable imperceptible sensing. When the microtube is compressed, the microchannel collapses, resulting in electrical discontinuity. We further developed a simple

wireless system to demonstrate a wearable fabric touch sensor capable of determining the position of forces acting on the fabric (Fig. 4F and Movie S4). Notably, we demonstrate high responsivity of the sensors (Fig. 4G), and we were able to recognize finger swiping directions by observing the activation patterns of the sensors. Overall, we demonstrate a facile method of developing a wearable fabric touch sensor of excellent flexibility, sensitivity, and responsivity.

Discussion

We describe a robust approach for the quick prototyping of 2D and 3D microfluidic devices using elastomeric microtubes of various sizes and cross-sections. To produce these microtubes, we use a continuous extrusion technique that only requires simple equipment and readily available materials. The continuous polymerization of thin liquid oligomer film around the filament by electric heating or UV light enables the production of very long microtubes with customizable ID and OD, making the technique scalable for mass production. By taking advantage of the flexibility of PDMS microtubes, we created valves and pumps as well as various 2D and 3D microfluidic assemblies with complex geometries, topologies, and functions. These architectures were fixed in position by using templates as guides for bending, shaping, and weaving. Typically, it took less than 1 min to assemble or reconfigure some of our complex devices, with precision in terms of channel layouts and performance of different functions (Movie S2). As such, this approach circumvents the limitations of conventional cleanroom-based microfabrication in the fast assembly of 3D systems and allows ease in configuring, modifying, and improving a prototype. Functional microfluidic elements, such as valves and pumps, may be easily adapted using off-the-shelf components. More complex geometries may be created by producing multiple lumens within the microtube. Importantly, this demonstrates the possibility of producing complex branched geometries that are ideal for simulating multiple-phase flows, or even mimicking blood capillaries.

The distinct circular channel shape is also advantageous in mimicking in vivo cardiovascular flow and has potential application in studying endothelization and microcirculation. The flexible

Fig. 4. Soft tubular microfluidics applications. (*A*) Time sequence events showing propulsion of microtubular robot based on catalytical reactions. The purple lines indicate tracking trajectories. (*B*) Plot showing effects of hydrogen peroxide concentration on speed of the microtubes. (*C*) Working mechanism of microtubular triboelectric sensor, with schematic diagram showing triboelectric and electrostatic inductions between liquid and microtube interface. (*D*) Peak-to-peak spiked triboelectric current produced at electrode as a function of log_{10}[KCl]. (*E*) Schematic showing microtubular touch sensor woven into a piece of fabric. (*Inset*) The actual microtube (red arrow) within the fabric. (*F*) Schematic shows wearable touch sensor communicating with a mobile app. (*G*) Electrical signal of the sensor when finger touches the different sensors independently, and then when swiping up or down.

microtubes form microfluidic devices that are soft and allow the fine-tuning of the circuit layout depending on needs, e.g., for focusing microentities of different sizes. We develop different microfluidic systems and components for inertial focusing of microparticles and microdroplet formation. Furthermore, as very low external pressures can cause large cross-sectional deformation of the elastic microtubes (42), we assembled our microtubes similar to Quake's multilayered valve configuration (8). The microtubes were arranged into switching valves and pumps and operated via pneumatic actuation. Moreover, the inherent building block characteristics of the elastic microtubes allow versatile configuration into complex microfluidic devices. By connecting the microtubes into networks, we generate microfluidic configurations with highly complex geometries and deterministic patterns over large areas. The microtubes may also be functionalized with biomolecules to serve as a micromotor. By using hydrogen peroxide as a fuel, microtubes can be altered to propel across the liquid medium. Biocatalytic enzymes may be deposited within the microtubular structure and modified to enable continuous propulsion. This can potentially serve as a drug carrier to targeted sites (32).

Additionally, their tiny footprint makes the microtubes excellent building blocks for the manufacture of wearable microfluidic sensors. The triboelectric property of the PDMS results in electrostatic interactions which may be used for electrochemical detection. The microtube could therefore be used as a fluid conduit, and has been shown to be useful in determining the ion concentrations of different liquids. Lastly, the PDMS microtube allows active sensing elements to be embedded inside, including liquid metals, ionic gels, or even 2D elements. Here, the thin PDMS wall thickness allows high deformability, which is especially suitable for force sensing. Furthermore, the thin sensors may be customized to different configurations to improve their sensitivity and specificity. Importantly, this potentially paves the way for imperceptible real-time health monitoring (42).

Taken together, the processes for this technique does not require significant engineering expertise or special facility to fabricate a 3D microfluidic device. This will address a number of disadvantages that are inherent to conventional microfabrication using soft lithography, such as cost incurred in iteration, low yield, and the restrictive planar manufacturing. Most importantly, this significantly lowers or even eliminates the technology barrier for more end users to participate in microfluidics research and shortens the path toward device commercialization.

Materials and Methods

The fabrication process involved using a customized setup as depicted in *SI Appendix*, Fig. S1. The OD of the elastomeric microtubes was controlled via the electrical heating period and pull-out speed. The metal wire and the polymeric microtube were separated in a sonication process in acetone solution, which washed off unreacted elastomer curing agent and caused slight swelling in the polymer, thereby loosening the polymer–metal contact. Other experimental procedures are detailed in *SI Appendix, SI Materials and Methods*.

1. Whitesides GM (2006) The origins and the future of microfluidics. *Nature* 442: 368–373.
2. Sackmann EK, Fulton AL, Beebe DJ (2014) The present and future role of microfluidics in biomedical research. *Nature* 507:181–189.
3. Bhatia SN, Ingber DE (2014) Microfluidic organs-on-chips. *Nat Biotechnol* 32:760–772.
4. Xu S, et al. (2014) Soft microfluidic assemblies of sensors, circuits, and radios for the skin. *Science* 344:70–74.
5. Whitesides GM (2013) Cool, or simple and cheap? Why not both? *Lab Chip* 13:11–13.
6. Au AK, Lee W, Folch A (2014) Mail-order microfluidics: Evaluation of stereolithography for the production of microfluidic devices. *Lab Chip* 14:1294–1301.
7. Duffy DC, McDonald JC, Schueller OJA, Whitesides GM (1998) Rapid prototyping of microfluidic systems in poly(dimethylsiloxane). *Anal Chem* 70:4974–4984.
8. Unger MA, Chou H-P, Thorsen T, Scherer A, Quake SR (2000) Monolithic microfabricated valves and pumps by multilayer soft lithography. *Science* 288:113–116.
9. Weaver JA, Melin J, Stark D, Quake SR, Horowitz MA (2010) Static control logic for microfluidic devices using pressure-gain valves. *Nat Phys* 6:218–223.
10. Xia YN, Whitesides GM (1998) Soft lithography. *Angew Chem Int Ed* 37:550–575.
11. Fiddes LK, et al. (2010) A circular cross-section PDMS microfluidics system for replication of cardiovascular flow conditions. *Biomaterials* 31:3459–3464.
12. Wong AD, Searson PC (2014) Live-cell imaging of invasion and intravasation in an artificial microvessel platform. *Cancer Res* 74:4937–4945.
13. Mecomber JS, Hurd D, Limbach PA (2005) Enhanced machining of micron-scale features in microchip molding masters by CNC milling. *Int J Mach Tools Manuf* 45:1542–1550.
14. Yuen PK, Goral VN (2010) Low-cost rapid prototyping of flexible microfluidic devices using a desktop digital craft cutter. *Lab Chip* 10:384–387.
15. Goral VN, Hsieh Y-C, Petzold ON, Faris RA, Yuen PK (2010) Hot embossing of plastic microfluidic devices using poly(dimethylsiloxane) molds. *J Micromech Microeng* 21:017002.
16. Kitson PJ, Rosnes MH, Sans V, Dragone V, Cronin L (2012) Configurable 3D-printed millifluidic and microfluidic 'lab on a chip' reactionware devices. *Lab Chip* 12:3267–3271.
17. Miller JS, et al. (2012) Rapid casting of patterned vascular networks for perfusable engineered three-dimensional tissues. *Nat Mater* 11:768–774.
18. Bhargava KC, Thompson B, Malmstadt N (2014) Discrete elements for 3D microfluidics. *Proc Natl Acad Sci USA* 111:15013–15018.
19. Ambrosi A, Pumera M (2016) 3D-printing technologies for electrochemical applications. *Chem Soc Rev* 45:2740–2755.
20. Lee J, Paek J, Kim J (2012) Sucrose-based fabrication of 3D-networked, cylindrical microfluidic channels for rapid prototyping of lab-on-a-chip and vaso-mimetic devices. *Lab Chip* 12:2638–2642.
21. Zhang W, et al. (2016) Elastomeric free-form blood vessels for interconnecting organs on chip systems. *Lab Chip* 16:1579–1586.
22. Quéré D (1999) Fluid coating on a fiber. *Annu Rev Fluid Mech* 31:347–384.
23. Sadd MH (2014) Two-dimensional problem solution. *Elasticity* (Academic, Boston), 3rd Ed, pp 159–234.
24. Au AK, Bhattacharjee N, Horowitz LF, Chang TC, Folch A (2015) 3D-printed microfluidic automation. *Lab Chip* 15:1934–1941.
25. Di Carlo D (2009) Inertial microfluidics. *Lab Chip* 9:3038–3046.
26. Goldsmith HL, Spain S (1984) Margination of leukocytes in blood flow through small tubes. *Microvasc Res* 27:204–222.
27. Kumar A, Graham MD (2012) Margination and segregation in confined flows of blood and other multicomponent suspensions. *Soft Matter* 8:10536–10548.
28. Zhang J, et al. (2014) Inertial particle separation by differential equilibrium positions in a symmetrical serpentine micro-channel. *Sci Rep* 4:4527.
29. Di Carlo D, Irimia D, Tompkins RG, Toner M (2007) Continuous inertial focusing, ordering, and separation of particles in microchannels. *Proc Natl Acad Sci USA* 104: 18892–18897.
30. Hou HW, et al. (2013) Isolation and retrieval of circulating tumor cells using centrifugal forces. *Sci Rep* 3:1259.
31. Teh S-Y, Lin R, Hung L-H, Lee AP (2008) Droplet microfluidics. *Lab Chip* 8:198–220.
32. Wang J, Gao W (2012) Nano/microscale motors: Biomedical opportunities and challenges. *ACS Nano* 6:5745–5751.
33. Tu Y, et al. (2013) Self-propelled supramolecular nanomotors with temperature-responsive speed regulation. *Nat Chem* 9:480–486.
34. Fan F-R, Tian Z-Q, Lin Wang Z (2012) Flexible triboelectric generator. *Nano Energy* 1: 328–334.
35. Li X, et al. (2015) Self-powered triboelectric nanosensor for microfluidics and cavity-confined solution chemistry. *ACS Nano* 9:11056–11063.
36. Chang H-C, Yeo LY (2010) *Electrokinetically Driven Microfluidics and Nanofluidics* (Cambridge Univ Press, Cambridge, UK), pp 35–75.
37. Zhu S, et al. (2013) Ultrastretchable fibers with metallic conductivity using a liquid metal alloy core. *Adv Funct Mater* 23:2308–2314.
38. Dickey MD (2017) Stretchable and soft electronics using liquid metals. *Adv Mater* 29: 1606425.
39. Yeo JC, Yu J, Koh ZM, Wang Z, Lim CT (2016) Wearable tactile sensor based on flexible microfluidics. *Lab Chip* 16:3244–3250.
40. Tang S-Y, et al. (2013) Electrochemically induced actuation of liquid metal marbles. *Nanoscale* 5:5949–5957.
41. Lazarus N, Hanrahan B (2016) Thermotherapy platform based on a highly stretchable wireless heater. *Adv Mater Technol* 1:1600130.
42. Xi W, Yeo JC, Yu L, Zhang S, Lim CT (2017) Wearable microtubular tactile sensor for real-time physiological pulse monitoring. *Adv Mater Technol* 2:1700016.
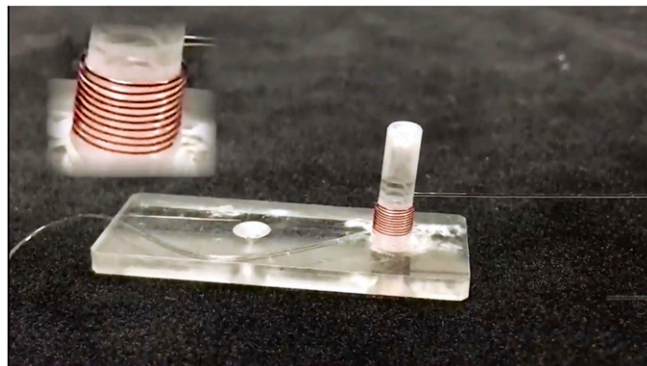
ENGINEERING

Supporting Information

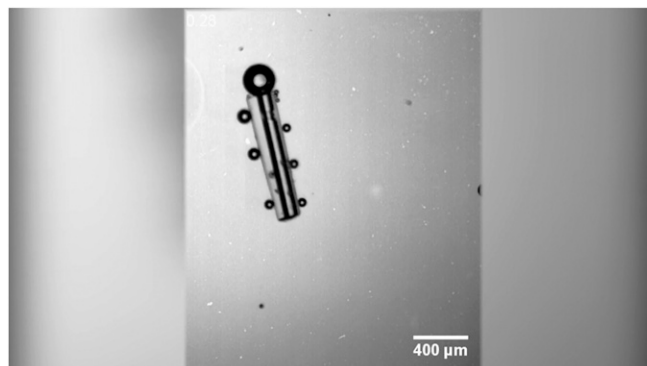## Xi et al. 10.1073/pnas.1712195114
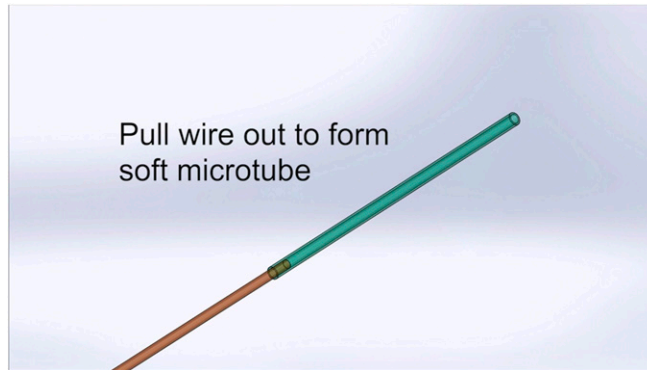
Movie S1.   The fabrication of soft microtube.
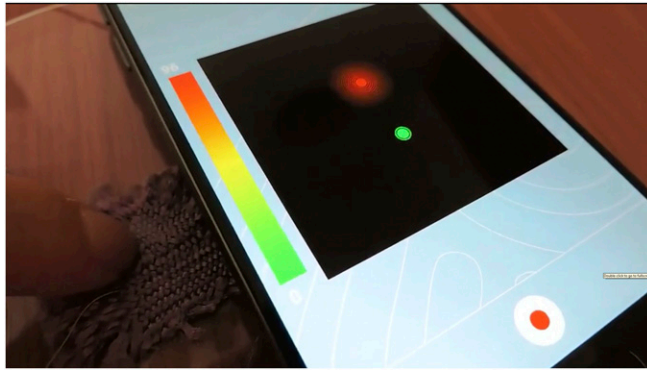
Movie S1

Movie S2.   The 2D and 3D STmF assembly.

Movie S2

Movie S3.   STmF for micromotor actuation.

Movie S3

Movie S4. STmF for wearable tactile sensing.

[Movie S4](#)

Other Supporting Information Files

[SI Appendix (PDF)](#)

Supporting Information

Xi et al. 10.1073/pnas.1712195114

SI Materials and Methods

Fabrication.

To fabricate PDMS microtubes, a metal wire (typically made of copper or tungsten) was vertically immersed into a freshly mixed PDMS (mixture of Sylgard 184 silicone elastomer base and Sylgard 184 silicone elastomer curing agent, 10:1 by weight) pool, as depicted in Fig. S1. The metal wire was then electrically heated up to ~100 °C. This generated a heat field close to the metal wire that initiated PDMS curing. A thin layer of cured PDMS formed around the wire and its thickness depended on the period of heating. When the metal wire was drawn out vertically above the liquid level, a second thin layer of viscous uncured PDMS was formed around the wire, which was further cured by hot air at ~95 °C in a cylindrical heating unit (Fig. S1). This generates a PDMS microtube enclosing the metal wire at the central axis. To produce a soft hollow tube, the metal wire was peeled off during a sonication process in acetone solution which washed off unreacted elastomer curing agent and caused slight swelling in the polymer, thereby loosening the PDMS-metal contact. The detached PDMS microtubes were then baked in an oven to remove any acetone remnant and stored for future use.

To fabricate microtubes from UV-curable polymer, a metal wire was pulled out of a pre-cured polymer (Mypolymer, MY-134-XP8, My Polymers Ltd.) pool into a glass chamber. Instead of electrical heating, the thin viscous polymer layer coated around the metal wire was cured on-site

under a UV mercury lamp. The peeling off procedure was done using a similar method as mentioned above. All the assembly work to fabricate microfluidic chips using PDMS microtubes was performed manually, guided with frameworks made by 3D printing or laser cutting.

Surface analyses.

For SEM imaging, the metal wires were fixed on a metal stage using double sided adhesive carbon tapes. The wires were observed using a JEOL scanning electron microscope (JSM-6010LV) with a 7 keV acceleration voltage. For the AFM analyses, the microtubes were cut into two halves from the midplane to expose the inner surfaces. The opened microtubes were then placed on a glass slide with the inner surface facing upward. The surface topography was characterized under ambient conditions by tapping mode AFM (JPK Instruments AG, Germany) at a scan rate of 0.5 Hz and images were acquired as 512×512 lines. The surface roughness analyses were subsequently extracted from the arithmetic average roughness (Ra), the root-mean-squared roughness (Rq) and the peak-to-valley height (Rm) measurements by evaluating the obtained AFM images.

Valving and actuation set-ups.

To make the valve, a PDMS microtube with an ID of 100 μm was mounted inside a laser-cut straight groove and a pincher was placed underneath to compress the microtube against a flat surface. The head of the pincher, which pinched the tube, has a width of 1mm. The pincher was then connected to a solenoid, which has an extension range of 2 mm and was controlled by a relay that was controlled by a digital signal generator. The solenoid responded to the digital signal to pinch (+5V) onto or release (0V) from the microtube with a maximum frequency of up to ~75 Hz.

The open and close states of the microtube were monitored by measuring the fluorescent intensity due to the aqueous fluorescein solution flowing in the microtube. The videos of valving behavior were recorded using an Olympus IX71 microscope with a high speed camera (Phantom v9, Vision Research Inc., USA) at a rate of 1000 images/second.

The peristaltic pump was installed with first mounting a PDMS microtube with ID = 100 μm as a pump tube onto a peristaltic pump (model P720, Instech Laboratories, Inc.) according to the P720 manual. The peristaltic pump was operated between 0.4 – 14 rpm and the motion of a column of water in the outlet tubing (0.5 mm ID) was used to calculate the pumping rate.

The formation of microchannels of arbitrary shapes.

The templates of circular, triangular, square, pentagonal, planar spiral, cylindrical and serpentine shapes that were used as guides to form different microtube patterns were fabricated either by 3D printing or laser cutting methods. The 2D and 3D channels were fabricated by bending or winding the PDMS microtubes into these templates.

Cell culture and seeding.

Madin-Darby Canine Kidney (MDCK) stable cell line expressing H1-GFP and HeLa cells were used. The cells were cultured in full Dulbecco's Modified Eagle Medium (DMEM, Sigma-Aldrich) supplemented with 1% antibiotics (penicillin/streptomycin, Invitrogen) and 10% Fetal Bovine Serum (FBS, Sigma-Aldrich) at 37 ℃ in a humidified atmosphere containing 5% CO_2. Human Umbilical Vein Endothelial Cells (HUVECs) were cultured in M-199 Medium (Sigma-Aldrich) supplemented with 20% FBS, 2 mmol/L penicillin/streptomycin, 2 mmol/L amphotericin

B, 2mmol/L L-glutamine, 10 mmol/L HEPES, 30-50 μg/ml endothelial cell growth supplement (Corning) and 100 μg/ml heparin sodium salt.

The cells were trypsinized and harvested at 70% confluence from culture flasks and re-suspended in the growth medium before seeding in the microtubes. Cell seeding into PDMS microtubes was performed by directly injecting a solution of 1×10^6 cells mL^{-3} into the microtubes, followed by culturing for $30 - 60$ minutes to allow cell attachment on the inner walls of the microtubes. This seeding procedure was repeated once after 180° rotation of the microtubes, which were subsequently submerged into full media for long-term culture. After 48 hours, cells were fixed using 4% paraformaldehyde for further imaging. For endothelial cells, the endothelialized PDMS microtubes were connected to a home-made microfluidic system and perfused with the growth medium at a flow rate of 50 μL/min for 48 hours before fixation. The fixed HUVECs in microtubes were stained with DAPI for confocal imaging. A Nikon confocal microscope equipped with a 20× objective was used to examine the cells in the microtubes. A z-stack of the entire tubular cell sheets was obtained at 1 μm per step. ImageJ (NIH) was then used to reconstruct the 3D tubular structure formed during epithelialization or endothelialization of the microtubes.

Microfluidics and image analysis.

Microfluidic assemblies formed from the microtubes were put together manually using 3D-printed supporting frames. The microtubes were connected to epoxy sealed blunt end tips (Fisnar Inc.) and solutions containing cells, blood or microparticles were routed into the microtubes using a syringe pump (NE-1000, New Era Pump Systems Inc., USA). To connect the microtube to an expanded outlet, a pulled glass capillary coated with a silane anti-adhesion layer was first inserted into the

microtube. The junction was later sealed by PDMS molding and the formation of the expanded channels in the outlet was obtained by pulling out the inserted glass capillary. Videos and images showing the flow at the outlet of the microtube-based devices were captured using an inverted epifluorescence microscope (Olympus IX71) equipped with a high speed camera (Phantom v9, Vision Research Inc., USA). The acquired high speed videos were then analysed using ImageJ (NIH) and Imaris 8.3.1 (bitplane) software to track individual micro-entities and calculate the focus efficiency, lateral distribution of microparticles and separation performance.

Designs of microchannels.

Microfluidic channels for focusing of microparticles were designed to enable inertial focusing behaviour. The effect of inertial focusing is closely relevant to the ratio between the particle diameter (a), the hydraulic diameter (D_h) (defined as the diameter in case of circular channels), the channel curvature and flow rate. The microtubes with a circular diameter of 100 μm were selected, as particles with sizes similar to that of cells (7 – 25 μm in diameter) were all above the stated a/D_h threshold of 0.07.

Physical adsorption of catalase into PDMS microtubes and optical imaging of locomotion.

A PDMS microtube with ID = 100 μm was injected with 100 μL of catalase solution (2 mg/mL) and incubated at 37 ºC overnight. The tube was cut into pieces of submillimeter in length and rinsed briefly with 1X PBS. These pieces were then placed into different hydrogen peroxide solution and imaged under an optical microscope. Videos of the locomotion were acquired by a high-speed camera (Photonic Science Limited) at 50 frames/s.

Triboelectric measurements.

A PDMS microtube with an ID = 100 μm and OD = 150 μm was used as a triboelectric sensor. A portion (~ 3 – 5 mm) at the middle of the microtube was coated with a layer of 20 nm Platinum by sputtering. This layer was later connected to a piece of tinfoil for better current conduction. A syringe pump was used to control the KCl solution movement inside the microtube and a programmable electrometer (Keithley 6517B) was adopted to detect the output current signal of the sensor.
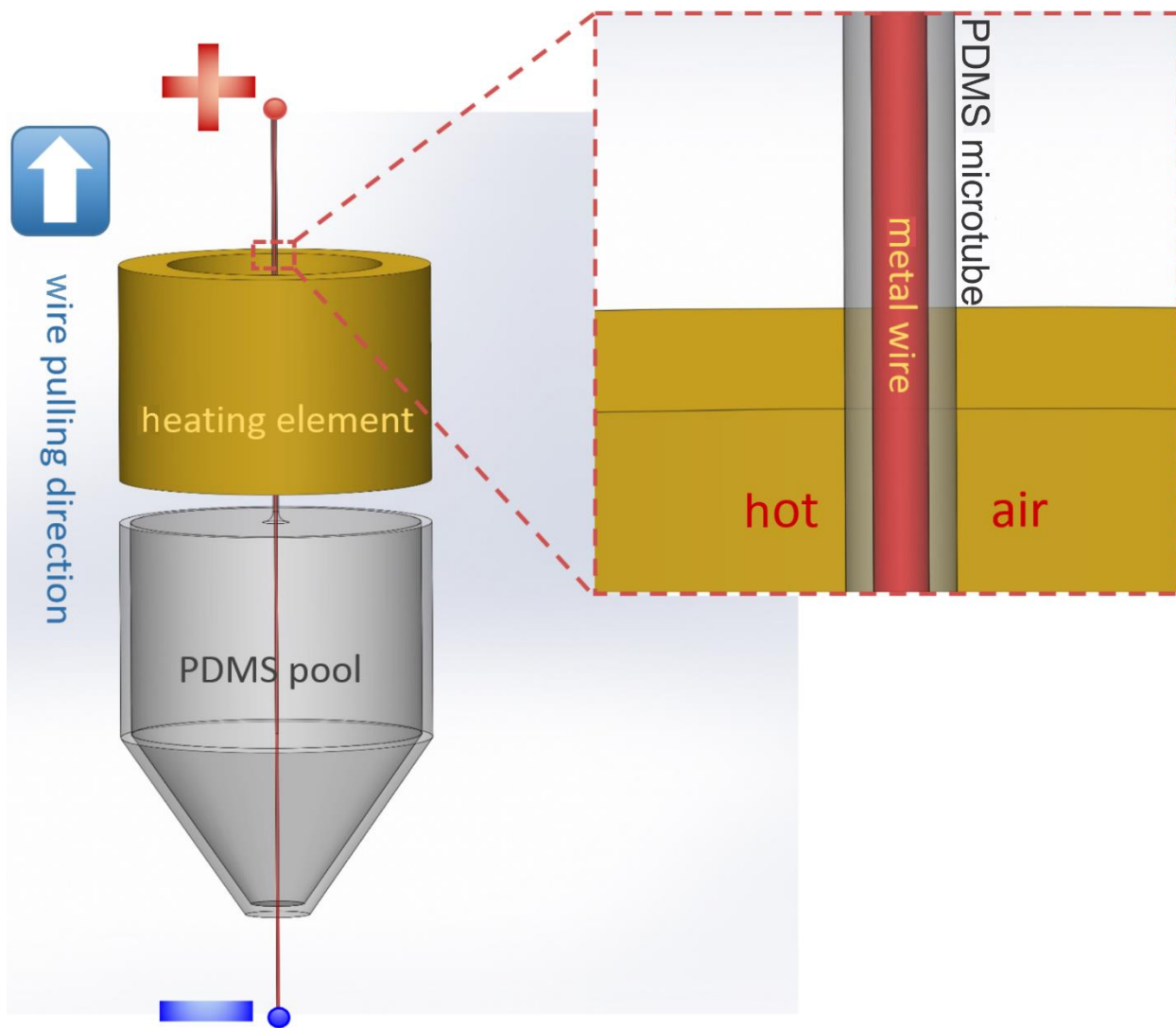
Fig. S1. Schematic view of the experimental set-up for fabrication of PDMS microtubes.
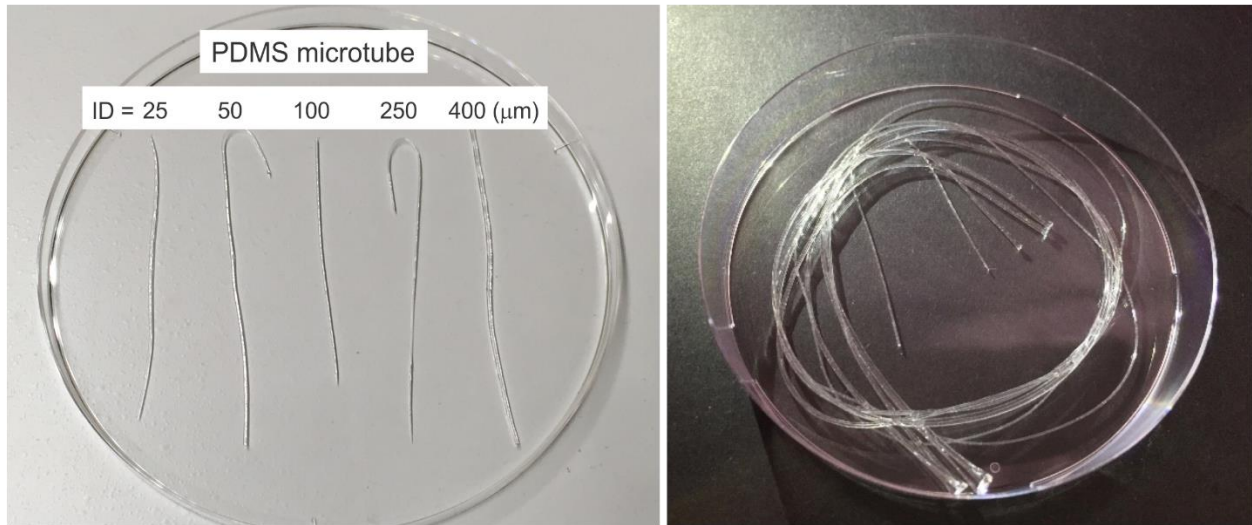
Fig. S2. Photos of (*A*) PDMS microtubes with different inner diameters (ID) and (*B*) left, a 45 cm long PDMS microtube with ID = 50 μm and right, the opening of the microtube (white arrow).
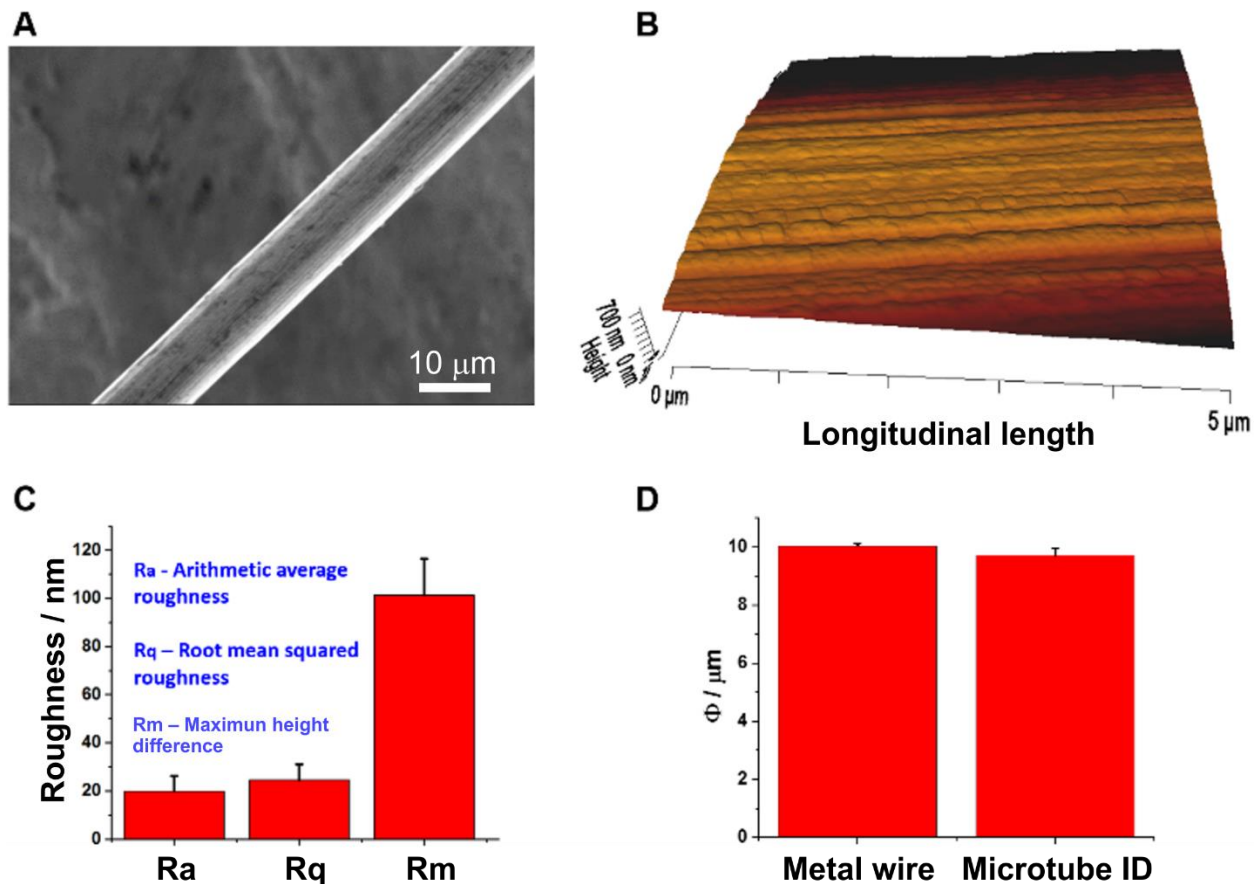
Fig. S3. (*A*) A SEM image showing a tungsten wire with diameter of 10 µm. (*B*) AFM topography showing the inner surface of a PDMS microtube (ID = 10 µm). (*C*) AFM roughness analysis of the inner surface of the microtube presented in (*B*). (*D*) The metal wire diameter and the ID of the PDMS microtube manufactured from the wire.
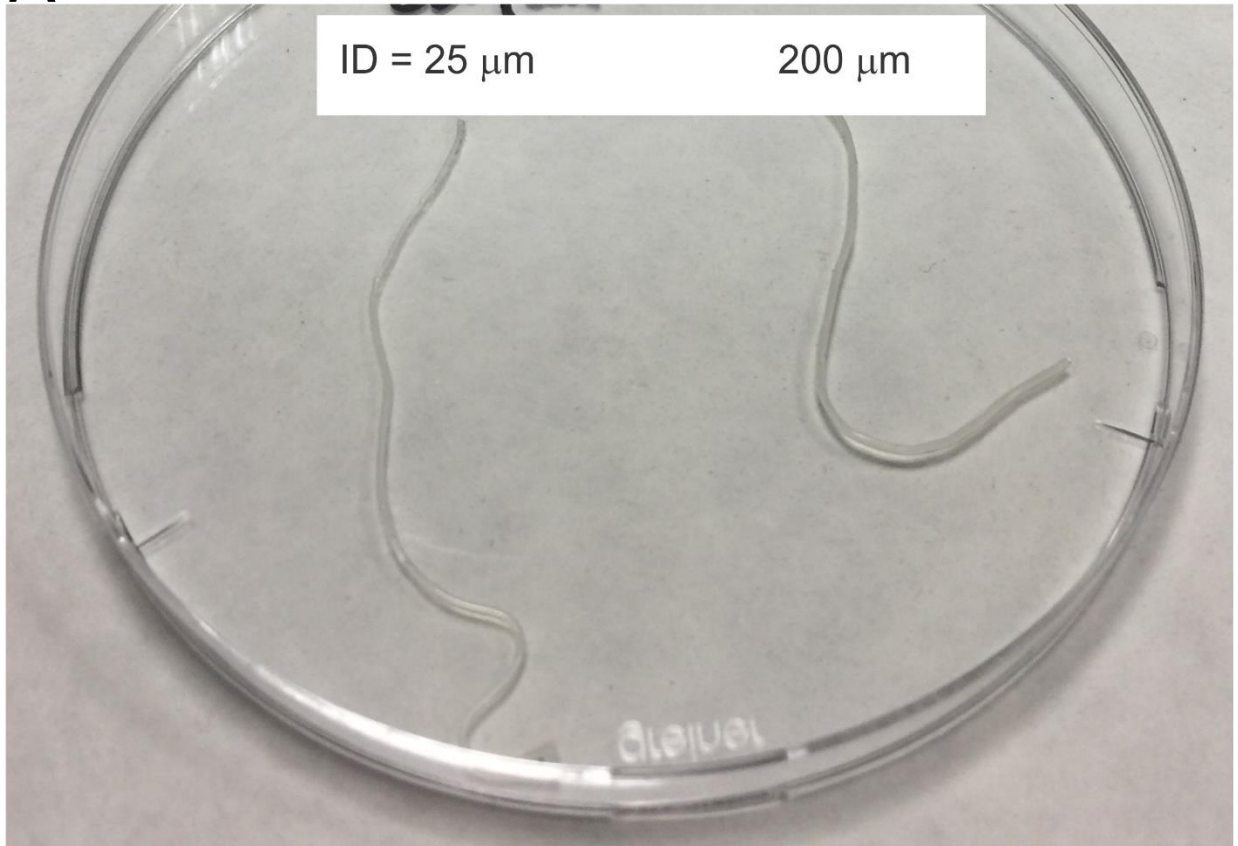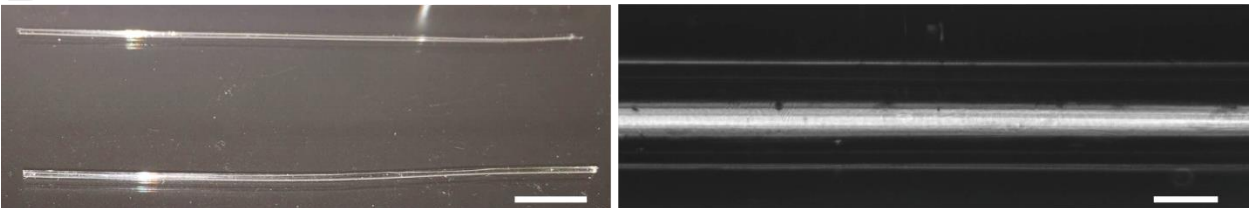
Fig. S4. (*A*) A photo shows two microtubes of different IDs made from Ecoflex® silicon rubber. (*B*) Two microtubes made from UV-curable polymer (left) and the optical image (right) showing the ID (250 µm) of the microtube. Scale bar: 5mm (left) and 150µm (right).
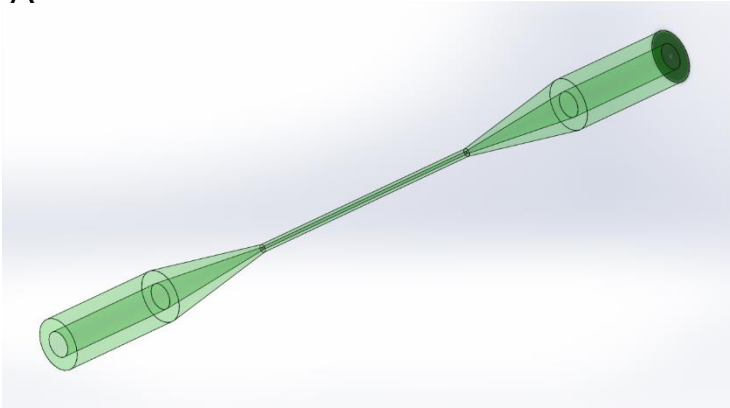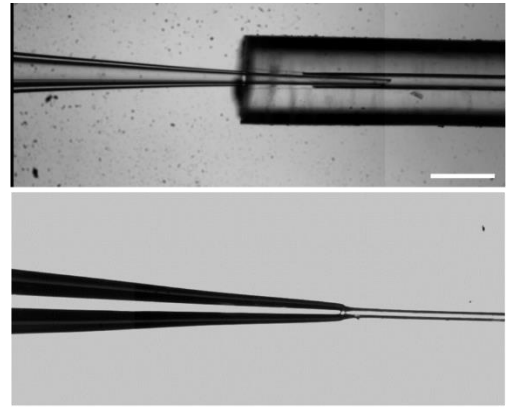
Fig. S5. (*A*) Schematic illustration showing a PDMS microtube with two expanded openings. (*B*) optical images showing top, inserted glass capillary as a template for opening expansion for a microtube of inner diameters (ID) = 25 μm, and bottom, the expanded opening that is compatible with commercially available blunt needles. Scale bar, 100 μm.

Table S1. The mechanical properties of the PDMS microtubes compared with commercially available silicone tubing.

Property	PTFE tubing	SEBS tubing	Our microtube
Minimum inner diameter (μm)	500	360	10
Tensile strength (MPa)	21 – 35	10	3 – 7
Elongation at break (%)	200 – 400	800 – 1000	200 – 400
Hardness (Shore)	D: 50 – 65	A:65	A: 43 – 50
Color	Opaque	Clear	Clear
References	Dow Corning Inc.	(1)	This work

1.   Zhu, S., et al., Ultrastretchable Fibers with Metallic Conductivity Using a Liquid Metal Alloy Core. Advanced Functional Materials, 2013. 23(18): p. 2308-2314.
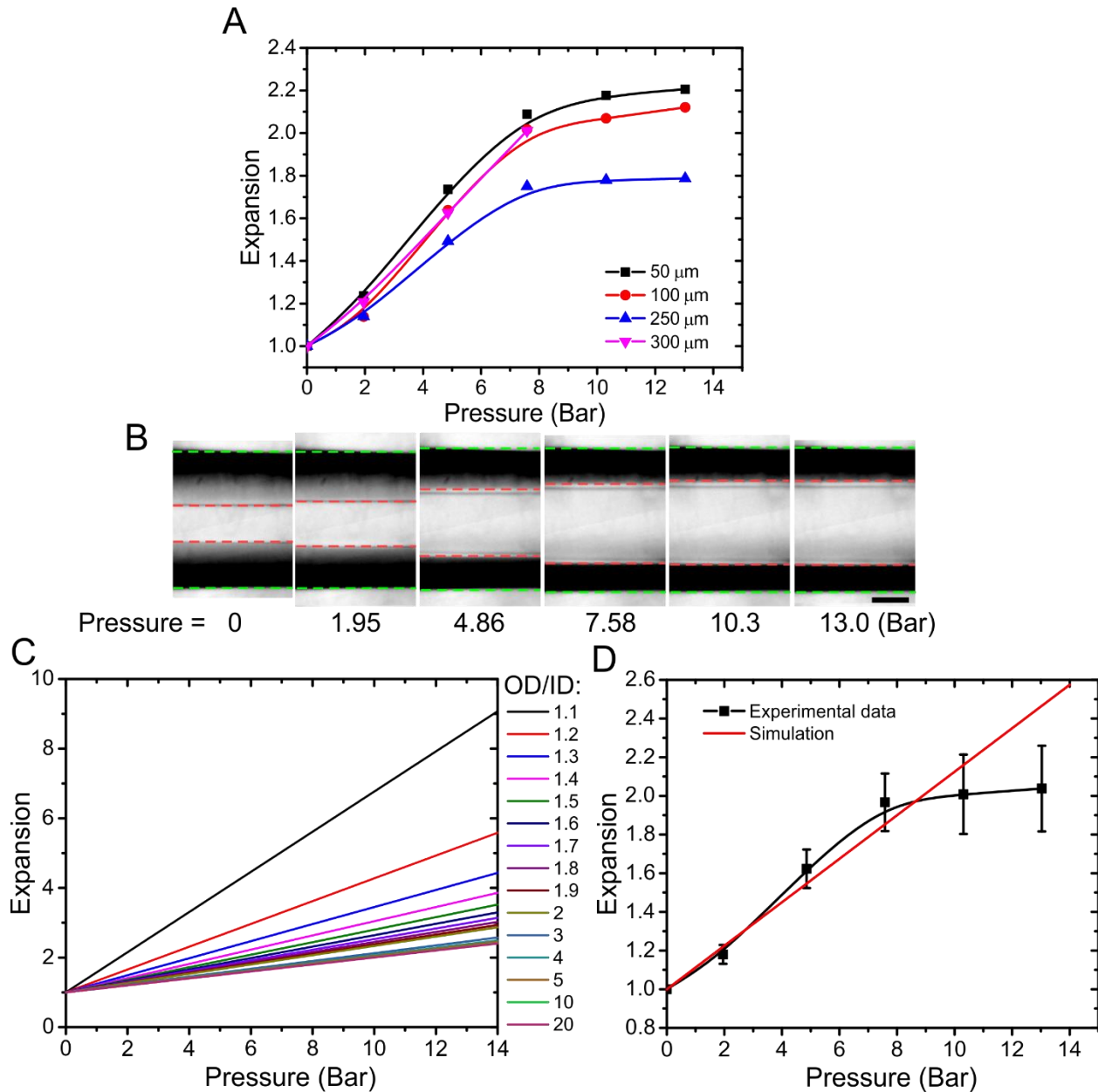
Fig. S6. (*A*) The normalized expansion of IDs of various microtubes as a function of intraluminal pressure. The IDs of the microtubes are listed in the lower right corner. The OD/ID ratio is one main factor that influences the expansion of the tubing. For all the microtubes, OD/ID = 3:1. (*B*) Optical images revealing the expansion of one PDMS microtube (ID = 50 μm and OD/ID = 3:1) as intraluminal pressure was increased. Red dash lines: inner wall; green dashlines: outer wall; scale bar: 50 μm. (*C*) Numerical analysis showing the linear expansion of perfect elastic tubes as a function of intraluminal pressure. (*D*) The experimental data for OD/ID = 3:1 is consistent with simulated expansion when pressure is smaller than 14 Bar.
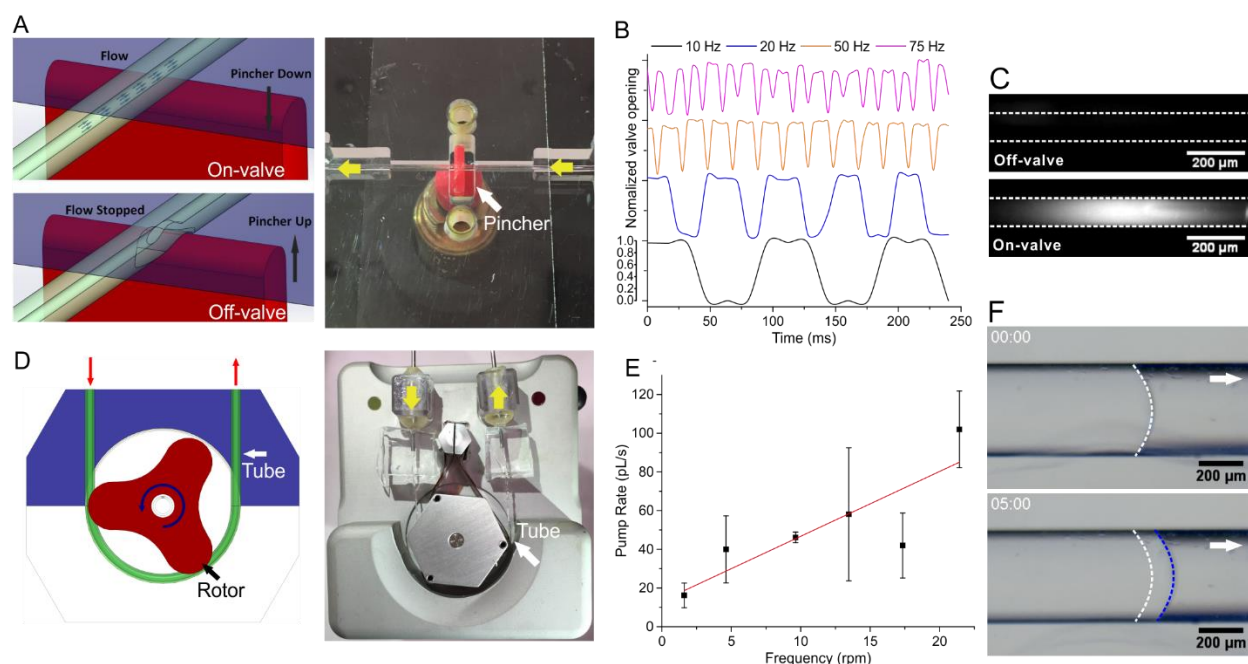
Fig. S7. Formation of microfluidic valve and pump with microtubes. (*A*) Schematic representation of an on-off valve. The valve is operated by periodically compressing a PDMS microtube with a mechanical pincer. Right, photo of the actual device. Yellow arrows indicate the microtube layout and the flow direction. White arrow indicates the position of the pincher. (*B*) The time response of opening and closing of a microtube (100 µm inner diameter) at different frequencies. The opening and closing of the microtube are measured by the intensity of the fluorescence inside the tube. (*C*) The normalized fluorescent intensity varying as a function of time is shown here. The abrupt increase and decrease in the fluorescent signal indicate a fast response of the microtube to the mechanical compression with minimum delay and the valve functions reasonably well up to 75 Hz, which is the limit of the solenoid. (*D*) Schematic representation of a peristaltic pump compressing a PDMS microtube (indicated by the white arrow) with ID = 100 µm. The rotor (the black arrow) occludes the flexible microtube and forces the fluid inside to be pumped through (the red arrows) as it turns (the blue arrow). Different pumping rates were achieved by rotating the rotor at various speeds. Right, photo of the actual device. Yellow arrows indicate flow direction. (*E*) Pumping rate of the peristaltic pump versus rotating speed. (*F*) Time lapse images showing the advancing fluid front in a time period of 5 minutes in the outlet of the peristaltic pump. White and blue dash lines show the advancement of the fluid front. White arrow indicates the flow direction.
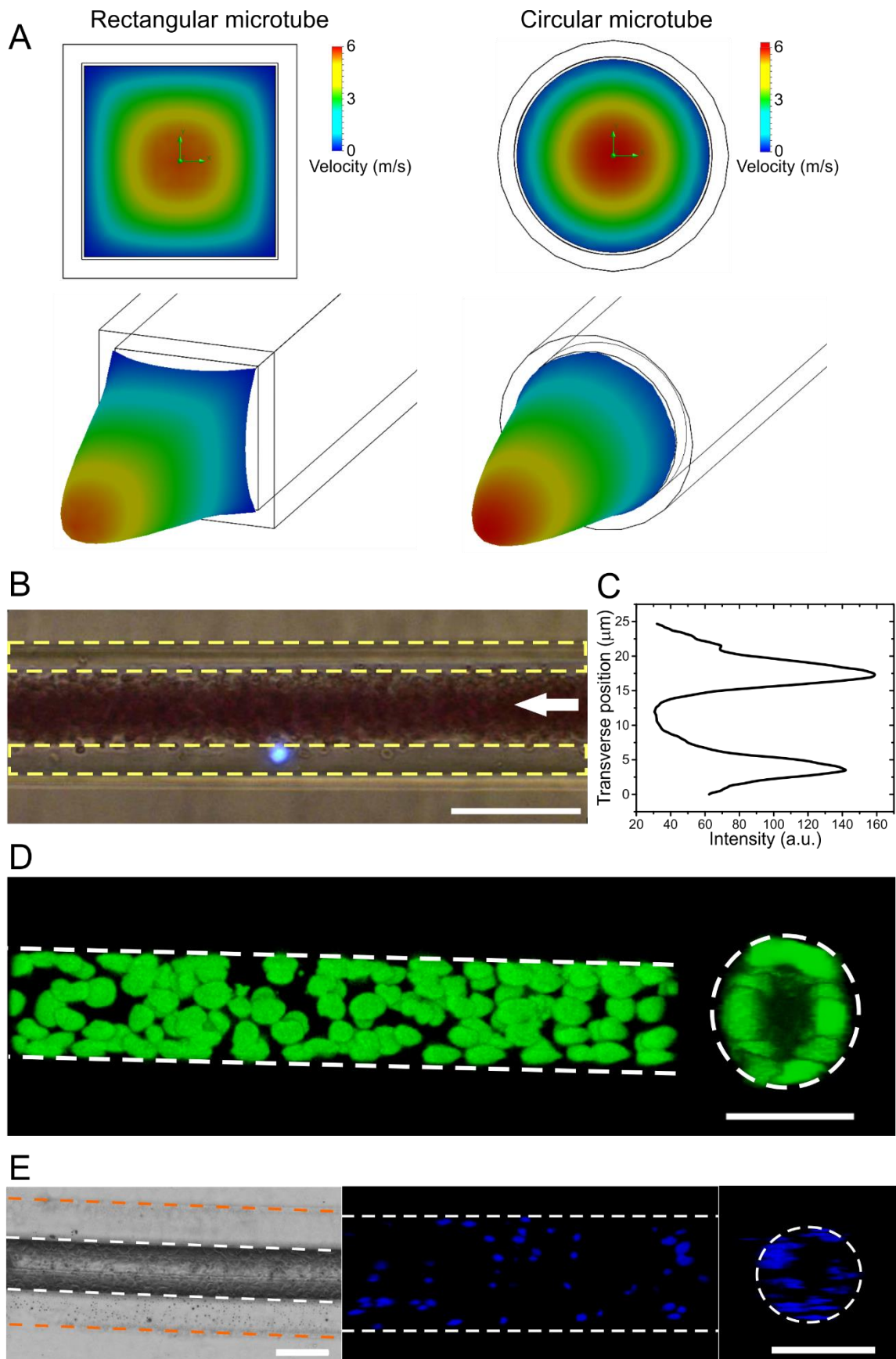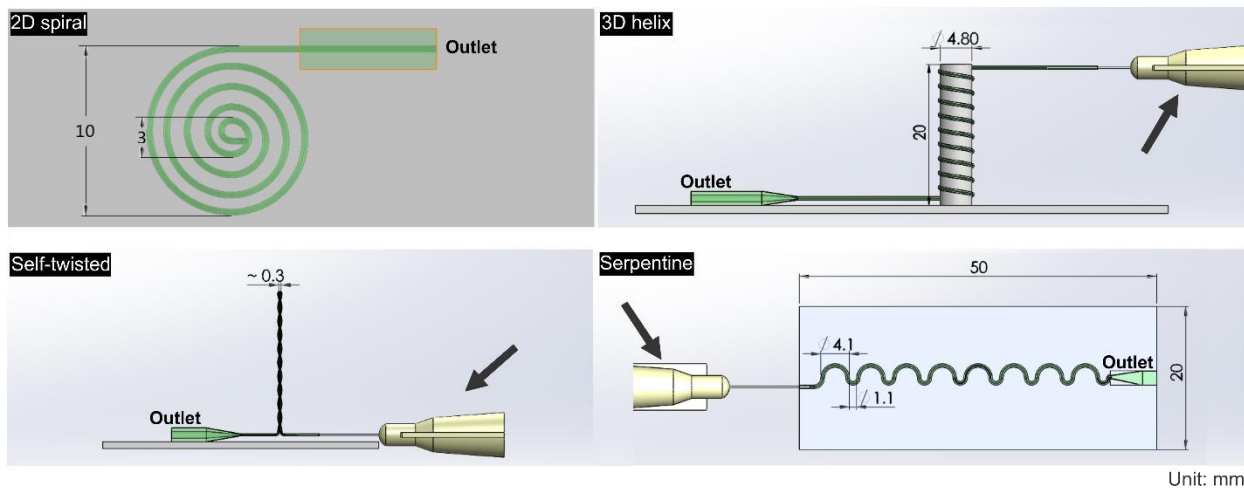
Rectangular microtube

Circular microtube

A

B

C

D

E

Fig. S8. Flow characteristics and cell functionalization inside circular microtubes. (*A*) Simulations of cross-sectional flow velocity profiles (2D profiles in upper panel and 3D profiles in lower panel, respectively) at outlets of a square microtube (left) and a circular microtube (right). The circular microtube (ID = 100 μm) and the square microtube have the same cross-sectional area. Other boundary conditions are: inlet/outlet pressure different is 1 Bar, and the lengths of the channels are 10 mm. (*B*) A typical optical image showing the margination effect of a HeLa cell in a circular microtube with ID = 25 μm. The white arrow indicates the flow direction and red blood cells (40% haematocrit in a whole blood sample) in the middle of the tube. The HeLa cells (stained blue due to DAPI staining) being positioned near to the cell-free plasma zone (as indicated by the yellow dash boxes) adjacent to the vessel wall is shown. Scale bar: 25 μm. (*C*) Fluorescent intensity profile, measured across the tubular channel in (*B*), demonstrates the HeLa cell distribution near the walls. (*D*) Fluorescent images of nuclei of epithelial cells (MDCK cells expressing H1-GFP) growing on the inner circumference (as indicated by the white dash lines) of a PDMS microtube (ID = 50 μm) for 24 hours, left: side view; right: cross-sectional view. Scale bars: 50 μm. (*E*) Bright field (left) and fluorescent images (DAPI; middle: side view and right: cross-sectional view) showing the growth of endothelial cells (HUVECs) on the inner wall (as indicated by the white dash lines) of a PDMS circular tube (ID = 100 μm). The orange dash lines indicate the outer surfaces of the tube. Scale bars: 100 μm.

Fig. S9. Schematic drawings of the different microtube-formed chips for micro-bead (polystyrene, Φ = 10, 15, 20 and 25 µm) focusing and separation. The microtubes used for these designs have an ID = 100 µm and an OD = 300 µm.
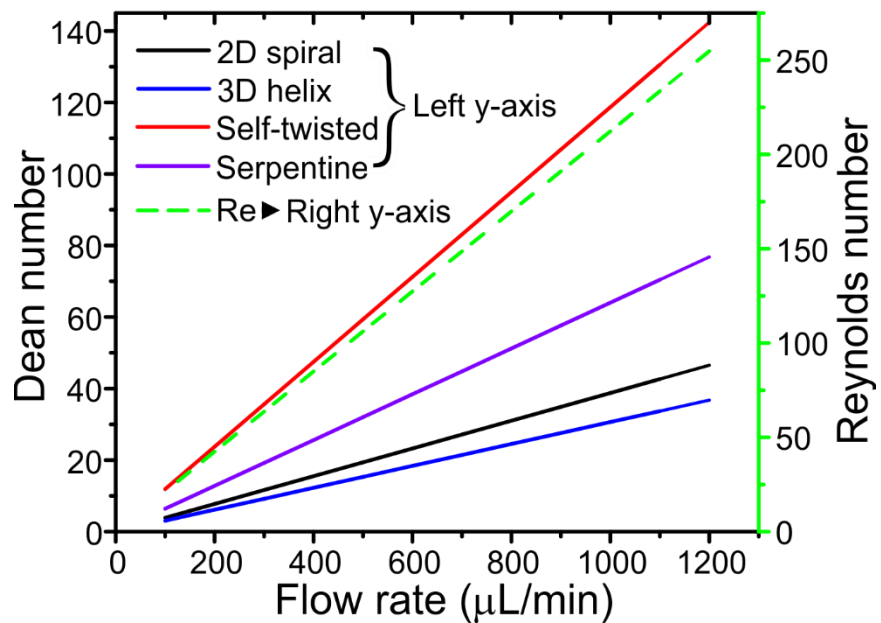
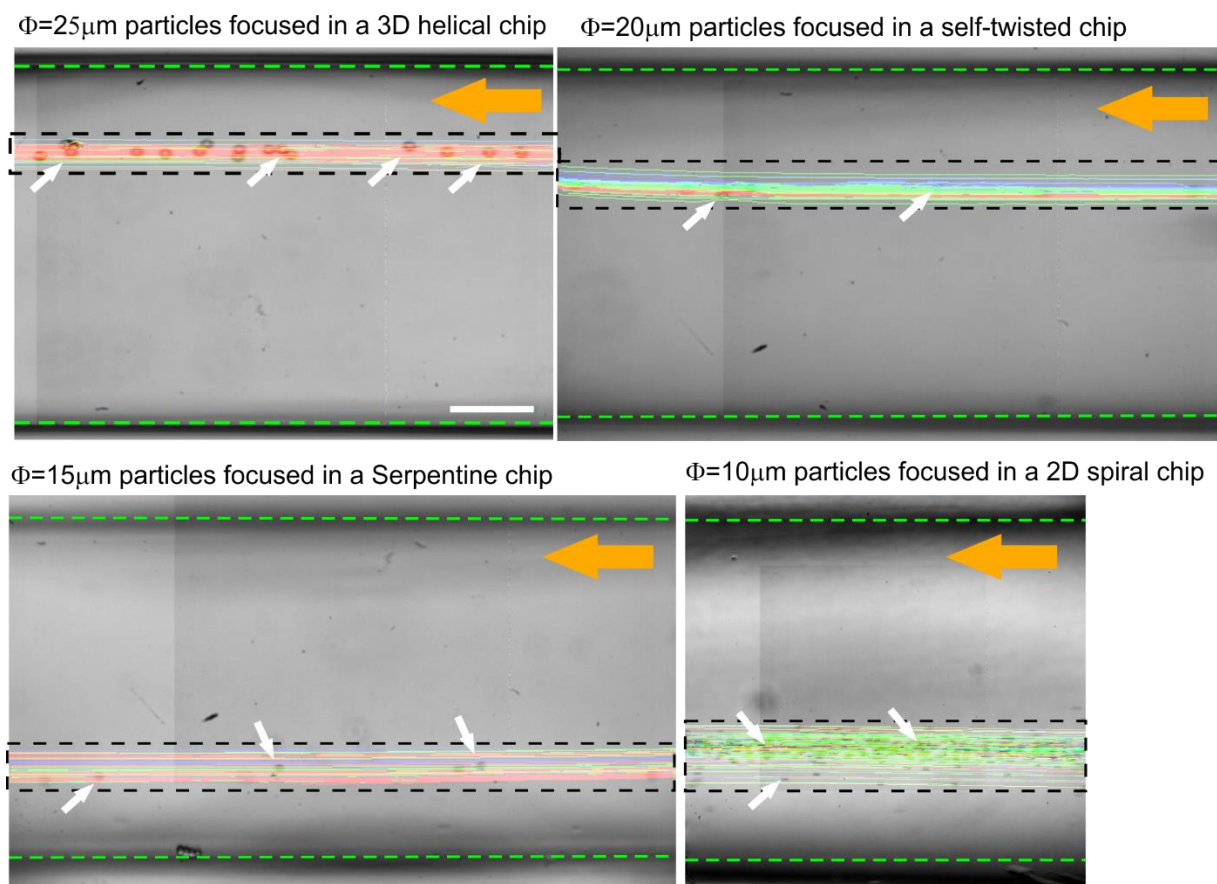**Fig. S10**. The calculated D_e and Re as a function of the flow rate for each configuration.

Fig. S11. Representative images showing focused microbeads (polystyrene, Φ = 25, 20, 15, and 10 μm) distribution at the outlets of chips of different configurations. The horizontal lines of different colours indicate tracking trajectories of the microparticles under flow. The width of the focused zones (indicated by the black dash boxes) is only ~10 to 20% the transverse dimension of the channels at the outlets. The orange arrows indicate the flow direction and the white arrows indicate the microparticles. Scale bar: 200 μm.
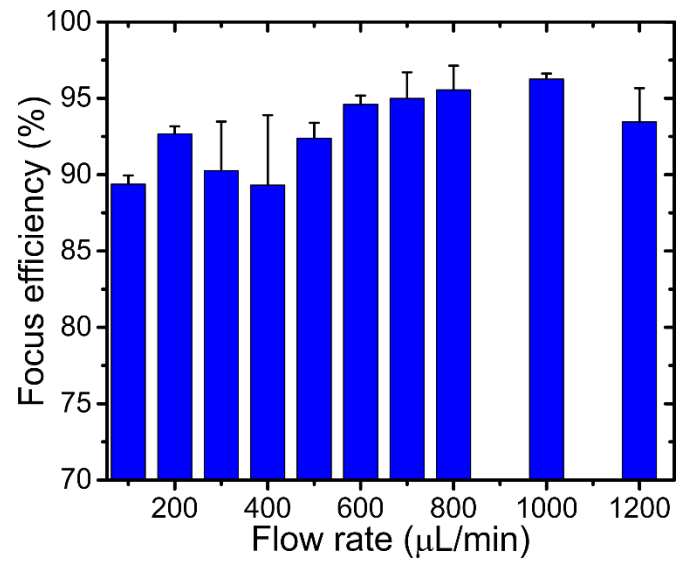
Fig. S12. Histogram of focus efficiency for microparticles (polystyrene, $\Phi = 25$ μm) in a 3D helical chip (Fig. S7) as a function of varying flow rates.
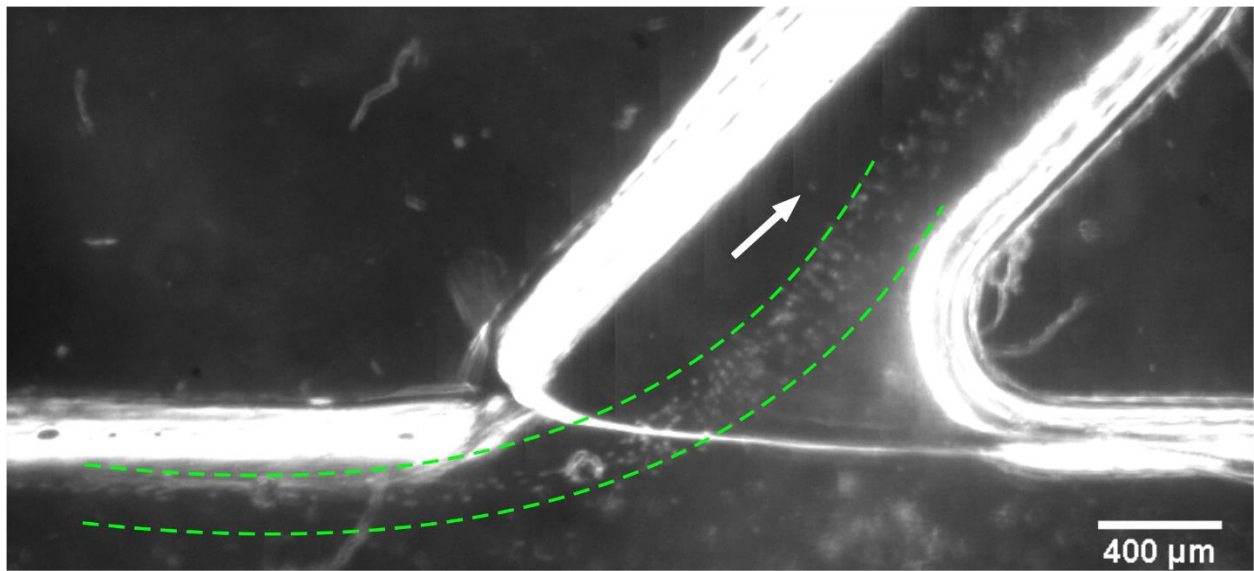
Fig. S13. MCF-10A cells (diameter ≈ 20 μm) focused to narrow streamlines and retrieved using 3D helical chip. The image showing the outlet of the device. White arrow indicates flow direction and focus zone is between green dash lines.
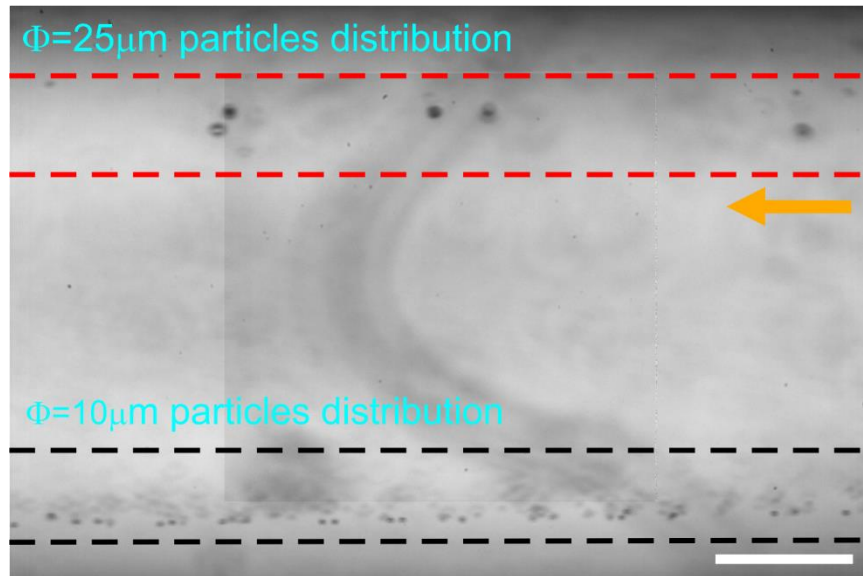
Fig. S14. Particles of 10 and 25 μm in diameter were focused into separate streamlines (between the black and red dash lines, respectively) in the outlet of a 3D helical chip. Scale bar: 150 μm.
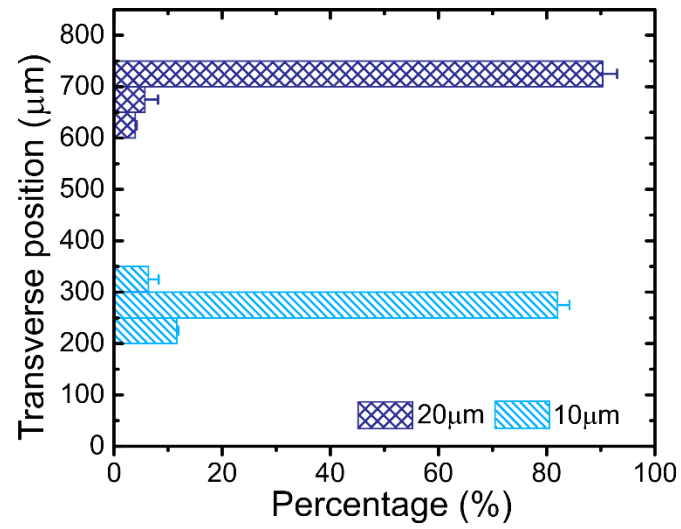
Fig. S15. Lateral position of polystyrene microparticles with diameters of 10 and 20 μm in the expanded outlet of a 3D helical chip.
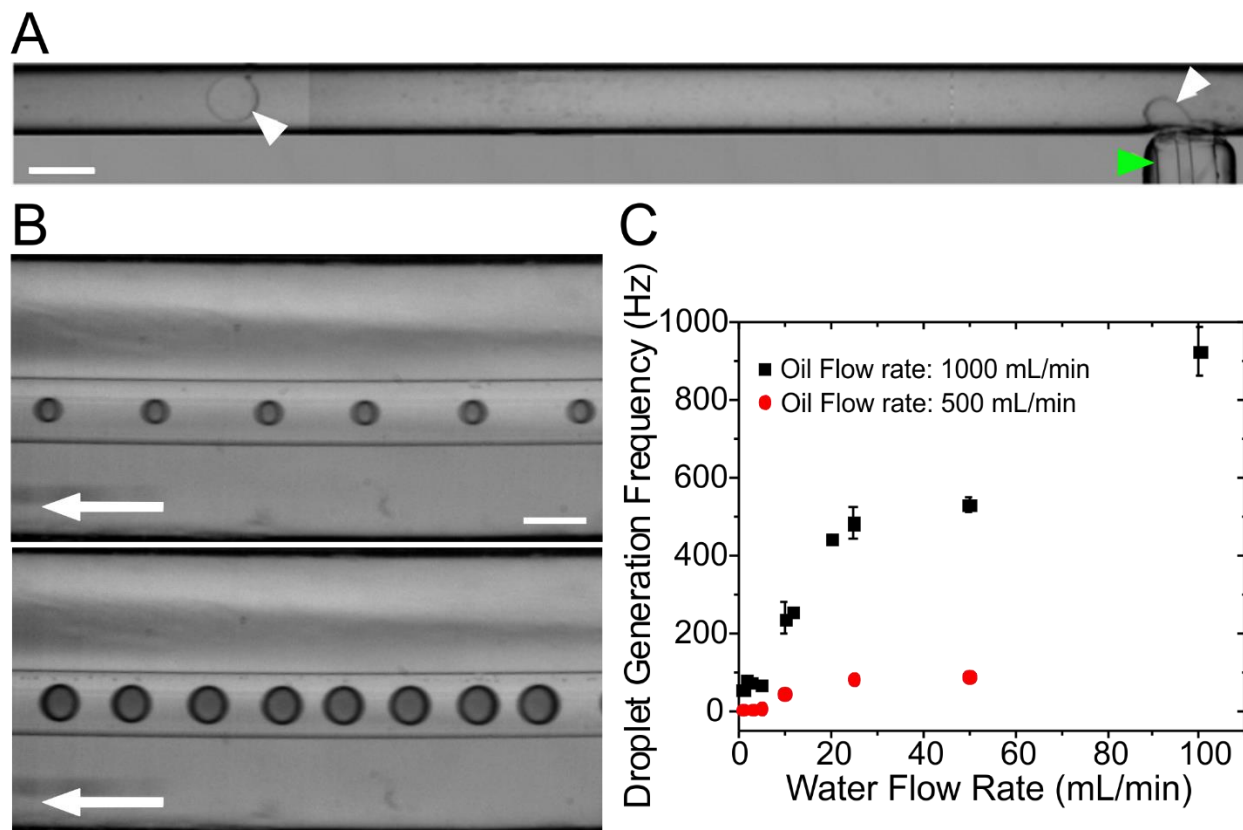
Fig. S16. Monodisperse water microdroplet generation in STmF chips. (*A*) A microtube (ID = 50 μm, green arrowhead) was inserted into a pre-made PDMS T-junction. Oil was flowing through the horizontal channel whereas water was flowing out of the microtube. This configuration enables generation of monodisperse microdroplets (here, water droplets indicated by the white arrowheads) in a high-throughput mode. Scale bar: 250 μm. (*B*) Optical images showing water droplets of a uniform diameter in a continuous oil flow (left image) and water droplets of changing diameters in an interrupted oil flow (lower image). The white arrows indicate the flow direction and scale bar: 250 μm. (*C*) Frequency of aqueous droplet generation as a function of the water flow rate for varied carrier phase flow rates of 1000 μl/min (black squares) and 500 μl/min (red circles).